Analysis of three-dimensional slope stability combined with rainfall and earthquake

Jiao Wang[1,2], Zhangxing Wang[1,2], Guanhua Sun[1,2], and Hongming Luo[1,2]

[1]State Key Laboratory of Geomechanics and Geotechnical Engineering, Institute of Rock and Soil

Mechanics, Chinese Academy of Sciences, Wuhan 430071, China;

[2]University of Chinese Academy of Sciences, Beijing 100049, China.

Correspondence: Hongming Luo (hmluo@whrsm.ac.cn)

Abstract

In the current context of global climate change, geohazards such as earthquakes and extreme rainfall pose a serious threat to regional stability. We investigate a three-dimensional(3D) slope dynamic model under earthquake action, derive the calculation of seepage force and the normal stress expression of slip surface under seepage and earthquake, and propose a rigorous overall analysis method to solve the safety factor of slopes subjected to combined with rainfall and earthquake. The accuracy and reliability of the method is verified by two classical examples. Finally, the effects of soil permeability coefficient, porosity and saturation on slope stability under rainfall in a project located in the Three Gorges Reservoir Area are analyzed. The safety evolution of the slope combined with both rainfall and earthquake is also studied. The results indicate that porosity has a greater impact on the safety factor under rainfall conditions, while the influence of permeability coefficient and saturation is relatively small. With the increase of horizontal seismic coefficient, the safety factor of the slope decreases

22 significantly. The influence of earthquake on slope stability is significantly greater than

23 that of rainfall. The corresponding safety factor when the vertical seismic action is

24 vertically downward is smaller than that when it is vertically upward. When considering

25 both horizontal and vertical seismic effects, slope stability is lower.

Keywords

Three-dimensional slopes; Rainfall; Earthquake; Stability analysis

1 Introduction

Rainfall-induced landslides are caused by the infiltration of precipitation into the ground surface, leading to an increase in pore water pressure, hence reducing the effective stress and shear strength of the soil. Sustained rainfall or heavy rainfall events can significantly increase the risk of slope instability, especially in those areas with loose, poorly drained soils. Several landslides in the Three Gorges reservoir area have been triggered by rainfall (Yin et al., 2012; Sun et al., 2016b). Earthquakes, as another key factor, impose additional dynamic loads on slopes through ground shaking, which may lead to instability of otherwise stable slopes. In addition, earthquake-induced landslides tend to be more destructive because they often occur without warning. Due to completely different destabilization mechanisms, studies of landslides induced by these two factors are often carried out separately. In some cases, rainfall and earthquakes may act together on slopes. And earthquake-induced landslides may occur more frequently during the rainy season, when the soil is saturated with water and its resistance to earthquakes is reduced. Further research is necessary to investigate the

43 stability of slopes under the combined influence of rainfall and earthquake (David, 2000;

44 Iverson, 2000; Sassa et al., 2010).

45   At present, the main research methods for slope stability include the limit

46 equilibrium method (Bishop, 1955; Morgenstern and Price, 1965; Spencer, 1967), limit

47 analysis (Farzaneh et al.,2008; Michalowski, 1995; Qin and Chian, 2018; Zhou et al.,

48 2017), Finite Element Method (Griffiths and Lane, 1999; Ishii et al., 2012) et al. There

49 have been numerous studies and findings regarding the stability assessment of 3D

50 slopes. However, most of these methods are based on extended 3D equilibrium analysis

51 techniques (Hungr, 1987; Zhang, 1988; Chen, 2001; Cheng and Yip, 2007), which

52 rarely strictly adhere to the six equilibrium conditions. Additionally, these approaches

53 often introduce a significant number of assumptions that limit their practical

54 engineering applications. The strict 3D limit equilibrium method proposed by Zheng

55 (2007) is an overall analysis approach based on the natural form of slip surface stress

56 distribution and approximation through shard interpolation. Sun et al. (2016a, 2017)

57 combined Morgenstern-Price and Bell global analysis method to analyze the stability

58 of reservoir bank slope, applying this method to the Three Gorges reservoir area.

59 Rahardjo et al. (2010) studied the effect of groundwater table position, rainfall

60 intensities, and soil properties in affecting slope stability using the numerical analyses.

61 Some of the defects inherent in the two-dimensional(2D) limit equilibrium method

62 remain unresolved, and some of them are even amplified in the complex 3D analysis,

63 which has a certain impact on the accuracy of the 3D slope stability evaluation. For the

As a common geological hazard in seismic zones, earthquake-triggered landslides

have been extensively investigated by numerous scholars (Sepúlveda et al., 2005;

Chang et al., 2012; Jibson and Harp, 2016; Marc et al., 2017; Salinas-Jasso et al., 2019).

At present, the stability analysis method of 3D slope is not mature, and the research on

the dynamic stability of 3D slope is even more scarce. The quasi-static method (Liu et

al., 2001) introduces coefficients (k_v and k_h) that reflect dynamic action, thereby

transforming a dynamic problem into a static one for easier resolution. This approach

avoids the complexities associated with dynamic analysis and has become widely used

in engineering. Horizontal seismic effects are often a significant consideration in slope

stability analysis, however, some research (Chopra, 1966; Lew, 1991; Ling et al., 1999;

Shukha and Baker, 2008) confirms that the vertical component of seismic forces should

also be given great attention. Wang and Xu (2005) employed the dynamic finite element

method to investigate the seismic response characteristics of various components in a

85 3D high slope yet failed to determine the safety factor. Guo et al. (2011) obtained the

86 time history curve of slope safety factor during earthquake using vector sum method in

87 2D situations. Cao et al. (2019) studied the seismic response and dynamic failure mode

88 of the slope subjected to earthquake and rainfall by two model tests. In summary,

89 although previous researches have provided significant insights into landslides

90 triggered by earthquakes, there remain inadequacies in fully considering the vertical

91 effects of seismic activity, extending analysis from 2D to 3D, and comprehensively

92 integrating the effects of both earthquakes and rainfall.

93   Most studies only consider the role of a single factor in seepage or earthquake,

94 neglecting the slope stability analysis under combined working conditions. Therefore,

95 analyzing the change law of safety factors for slopes during seepage and seismic action

96 is of great practical value in guiding slope support design and evaluating slope stability.

97 In this paper, a 3D rigorous slice-free method considering seepage and seismic forces

98 to solve the safety factor of bank slopes is proposed. The proposed method strictly

99 satisfies the force balance and moment balance in three directions, without introducing

100 other redundant assumptions.

101 **2 Rise of phreatic surface and calculation of seepage force with rainfall**

102 **infiltration in the soil column**

103   The phreatic surface is the interface between the saturated and unsaturated zones

104 within the slope. Physical and mechanical parameters of the sliding below the phreatic

105 surface adopt saturated, while above the phreatic surface adopt naturally. A differential

106   soil slice is taken from the slip surface to the slope surface in the landslide body is

107   shown in Fig. 1. $z(t)$ is the rise of phreatic surface after rainfall infiltration, which

108   refers to Conte and Troncone (2017), the height of the soil slice below the phreatic line

109   on BE and CF side are respectively z_1 and z_2. It is assumed that rainfall is consistent

110   with groundwater movement and that the slope surface is well drained and free of

111   standing water. Regardless of rainfall intensity, runoff will form if it is greater than the

112   infiltration capacity. The height of rise of the phreatic surface within the slope after the

113   rainfall is

$$z(t) = \frac{z_r}{n(1-S_r)} \exp\left[-\frac{k}{ds\cos\alpha}i\cos\delta\left(t-t_0\right)\right] \tag{1}$$

114

115   where z_r is the volume of water (per unit area) that infiltrates the slope due to a

116   rainfall event with a specified duration, n is porosity, k is permeability coefficient, S_r

117   is saturation, i is the hydraulic gradient ($i = \sin\beta$), δ is the angle between the slope

118   surface and the horizontal plane, α is the angle between the sliding surface BC of the

119   differential soil slice and the horizontal plane, β is the angle between the phreatic line

120   and the horizontal plane, ds is the length of the sliding surface BC of the differential

121   soil slice, t is time, and t_0 is the initial moment. As a further simplification, it is

122   assumed that both n and S_r are constant.
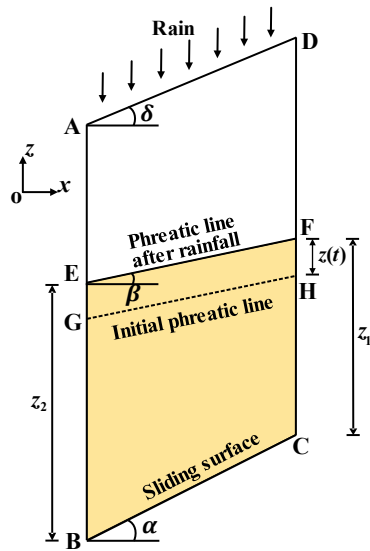
123

124   **Fig. 1** Relationship between rainfall and groundwater level
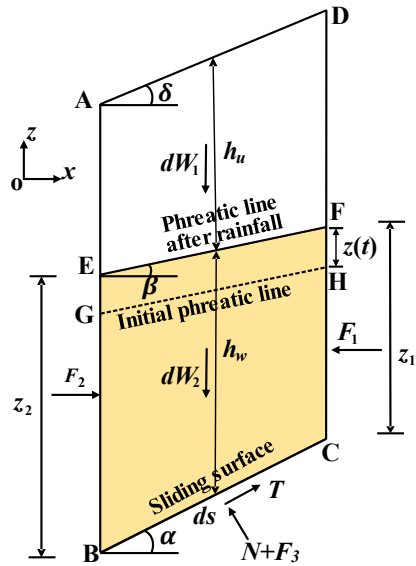
125

126   **Fig. 2** Calculation sketch of forces acting on the differential soil slice
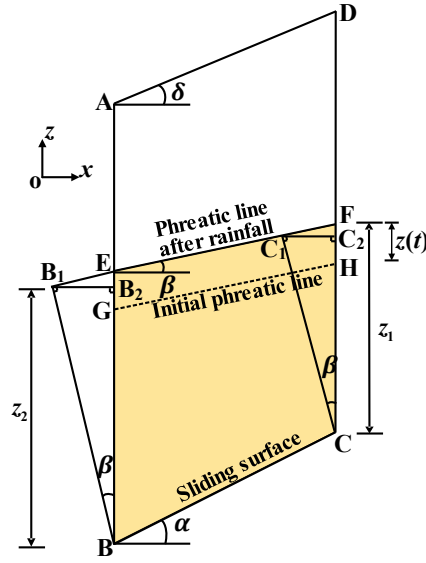
Fig. 3 Calculation sketch of hydraulic head

The load on the soil slice is shown in Fig. 2. dW_1 and dW_2 are the gravity of the differential soil slice above and below the phreatic line. The resultant hydrostatic force of the boundary *AB*, *CD*, and *BC* are F_1, F_2, and F_3 respectively. *N* is the contact pressure (effective pressure) between the soil particles, and *T* is the sliding resistance force. h_u and h_w are the height of the soil slice above and below the phreatic line respectively.

According to the flow properties of the phreatic line perpendicular to the equipotential line, the surrounding hydrostatic pressures F_1, F_2, and F_3 on the boundary *CF*, *BE*, and *BC* can be determined. As shown in Fig. 3, BB_1 and CC_1 are perpendicular to the phreatic line, then make B_1B_2 perpendicular to *AB*, and C_1C_2 perpendicular to *CD*. According to the geometric relationship, the hydrostatic pressure resultant forces at the boundary *CF* and *BE* are

$$F_1 = \frac{1}{2}\gamma_w z_1{}^2 cos^2\beta, F_2 = \frac{1}{2}\gamma_w z_2{}^2 cos^2\beta \qquad (2)$$

142   γ_w is the unit weight of the water. Let $h_w = \frac{1}{2}(z_1 + z_2)$, the hydrostatic pressure

143   resultant force on the slip surface BC is

$$F_3 = \frac{1}{2}\gamma_w(z_1 + z_2)ds\cos^2\beta = \gamma_w h_w ds\cos^2\beta \tag{3}$$

145   The components of F_3 in the horizontal and vertical directions are

$$U_x = \gamma_w h_w ds\cos^2\beta\cos\alpha, \quad U_y = \gamma_w h_w ds\cos^2\beta\sin\alpha \tag{4}$$

147   The gravity of water in differential soil slice is

$$dW_{2w} = \gamma_w h_w ds\cos\alpha \tag{5}$$

149   The permeability pressure is a pair of balancing forces with the water weight in a

150   differential soil slice and the hydrostatic pressure around it (Zheng et al., 2004).

151   Therefore, the weight of water in the differential soil slice and the surrounding

152   hydrostatic pressure can be replaced by a seepage force. The force diagram in Fig. 2

153   can be replaced by Fig. 4. dW_2' represents the effective unit weight of the soil below

154   the phreatic line and dW_D is the seepage force.
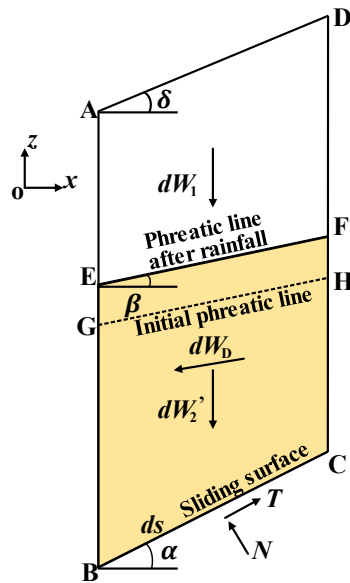
156   **Fig. 4** Simplified force diagram on a differential soil slice

157   The horizontal and vertical component of the seepage force dW_3 are

$$dW_{Dx} = F_1 - F_2 + U_x = \gamma_w h_w cos^2\beta(z_1 - z_2 + dssin\alpha) \tag{6}$$

159

$$dW_{Dy} = dW_{2w} - U_y = \gamma_w h_w dscos\alpha sin^2\beta \tag{7}$$

160   According to geometric relation

$$z_1 - z_2 + dssin\alpha = dscos\alpha \tan\beta \tag{8}$$

162   Therefore, the seepage force is

$$dW_D = \gamma_w h_w dscos\alpha \sin\beta \tag{9}$$

164   The direction of seepage force is consistent with groundwater flow. The direction

165   of groundwater flow within the sliding soil mass is determined by the inclination of the

166   phreatic surface in each differential soil slice. As shown in Fig. 4, the flow direction of

167   groundwater is oriented at an angle β relative to the horizontal plane.

168   3 A global analysis method for slope stability under seepage and

169   earthquake

170   3.1 Overall system of equilibrium equations

171   As shown in Fig. 5, taking the whole sliding body Ω as the research object, and

172   S is a potential slip surface.
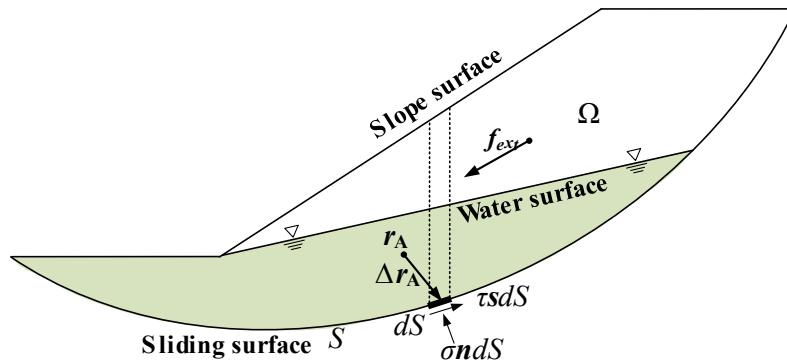
174   **Fig. 5** A 2D schematic plot for force system in/on the sliding body

175 dS is a differential element on the sliding surface S. The normal force on a

176 differential element dS at point $\boldsymbol{r}$ is $\sigma \boldsymbol{n} dS$, the resultant shear force is $\tau \boldsymbol{s} dS$, $\boldsymbol{n}$ is

177 the unit normal vector at position vector $\boldsymbol{r}$ on S and pointing to the inside of the sliding

178 body Ω; $\boldsymbol{s}$ is the unit tangent vector at position vector $\boldsymbol{r}$ on S and opposed to the

179 sliding direction of the sliding body Ω, so the reaction on dS is:

180
$$d\boldsymbol{f} = (\sigma \boldsymbol{n} + \tau \boldsymbol{s}) dS \tag{10}$$

181
$$d\boldsymbol{m}_A = \Delta \boldsymbol{r}_A \times d\boldsymbol{f} \tag{11}$$

182 Here, $\Delta \boldsymbol{r}_A = \boldsymbol{r} - \boldsymbol{r}_A$, $\boldsymbol{r}$ is the position vector of dS, $\boldsymbol{r}_A$ is the position vector for any

183 given reference point A, "$\times$" represents vector multiplication.

184 $\boldsymbol{f}_{ext}$ is the resultant external force vector, including external loads such as gravity,

185 seepage force, seismic force, et al.; $\boldsymbol{m}_{ext}$ denotes the moment $\boldsymbol{f}_{ext}$ concerning $\boldsymbol{r}_A$. To

186 integrate over the entire sliding surface dS:

187
$$\iint_S d\boldsymbol{f} + \boldsymbol{f}_{ext} = \boldsymbol{0} \tag{12}$$

188
$$\iint_S d\boldsymbol{m}_A + \boldsymbol{m}_{ext} = \boldsymbol{0} \tag{13}$$

189 According to Mohr-Coulomb criterion,

190
$$\tau = \frac{1}{F_s}\left[c' + f'(\sigma - u)\right] = \frac{1}{F_s}\left(c_w + f'\sigma\right) \tag{14}$$

191 Here, F_s is the safety factor, c' and f' are the effective stress shear strength

192 parameters, c' is cohesion, f' corresponds to the tangent of the friction angle, u is

193 the pore pressure; c_w is defined as

194
$$c_w \equiv c' - f'u \tag{15}$$

195 Order,

196
$$n' = \begin{pmatrix} n \\ \Delta r_A \times n \end{pmatrix}, \quad s' = \begin{pmatrix} s \\ \Delta r_A \times s \end{pmatrix}, \quad f_m = \begin{pmatrix} f_{ext} \\ m_{ext} \end{pmatrix} \tag{16}$$

197   Substituting equations (10), (11), and (14) into equations (12) and (13), and

198   merging into a more compact form:

199
$$F_s \left(\iint_s n' \sigma dS + f_m \right) + \iint_s \left(c_w + f'\sigma \right) s' dS = 0 \tag{17}$$

200   **3.2 Normal stress expression of slip surface under seepage force and seismic force**

201   As shown with the dash line in Fig. 5, a vertical differential cylinder is now taken

202   from the homogeneous sliding body from the slip surface to the slope surface. The load

203   on the differential cylinder is shown in Fig. 6. $-kdw_1$ is the weight of the soil above

204   phreatic surface, and $-kdw_2'$ refer to the floating weight of the soil below the phreatic

205   surface. pdw_3 and edw_4 denote the seepage force and seismic force. dh refers to the

206   action force of the soil around the differential cylinder.
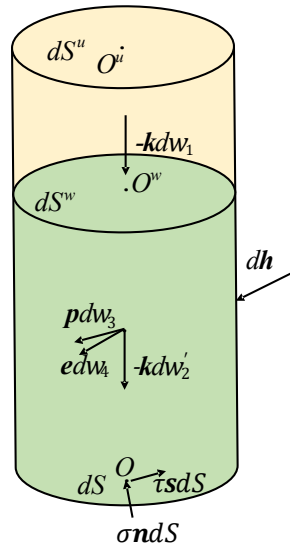
208   **Fig. 6** Sketch of force acting on a vertical differential cylinder in a sliding body

209   Here, k = unit vector of z-axis; p = unit vector pointing to the direction of the

210   seepage force; e = unit vector pointing to the direction of the seismic force; θ = angle

211   between dS and the horizontal plane; ξ = angle between the phreatic surface dS^w and

212   the horizontal plane in the differential cylinder.

213   The force equilibrium condition for a differential cylinder is

214     $$\sigma \boldsymbol{n} dS + \tau \boldsymbol{s} dS - \boldsymbol{k} dw_1 - \boldsymbol{k} dw_2' + \boldsymbol{p} dw_3 + \boldsymbol{e} dw_4 + d\boldsymbol{h} = \boldsymbol{0} \tag{18}$$

215   Both sides of the Eq. (18) are simultaneously multiplied by $\boldsymbol{n}$ to obtain

216     $$\sigma = n_3 \left(\frac{dw_1}{dS} + \frac{dw_1'}{dS} \right) - n_p \frac{dw_3}{dS} - n_e \frac{dw_4}{dS} - \frac{\boldsymbol{n} \cdot d\boldsymbol{h}}{dS} \tag{19}$$

217   Here, n_3 = component of $\boldsymbol{n}$ in the positive direction of z-axis, n_p = projection of

218     $\boldsymbol{p}$ in $\boldsymbol{n}$ direction, n_e = projection of $\boldsymbol{e}$ in $\boldsymbol{n}$ direction.

219   Known,

220
$$\begin{cases} dw_1 = \overline{\gamma} H_u dS \cos\theta \\ dw_2' = \overline{\gamma'} H_w dS \cos\theta \\ dw_3 = \gamma_w H_w dS \cos\theta \sin\xi \\ dw_4 = k_c \left(\overline{\gamma} H_u + \overline{\gamma}_{sat} H_w \right) dS \cos\theta \\ n_p = \boldsymbol{n} \cdot \boldsymbol{p} \\ n_e = \boldsymbol{n} \cdot \boldsymbol{e} \end{cases} \tag{20}$$

221   where, $\overline{\gamma}$ = average value of the unit weight of the soil above the phreatic surface; γ'

222   = average value for the unit floating weight of the soil below the phreatic surface; $\overline{\gamma}_{sat}$

223   = average value of the unit saturated weight of below the phreatic surface; γ_w = unit

224   weight of water; H_u = height of soil above the phreatic surface; H_w = height of the soil

225   below the phreatic surface; k_c = seismic force coefficient.

226   Substitute Eq. (20) into Eq. (19) and sort it out

227     $$\sigma = (\gamma H_u + \gamma' H_w) \cos^2\theta - n_p \gamma_w H_w \cos\theta \sin\xi - n_e k_c \left(\gamma H_u + \gamma_{sat} H_w \right) \cos\theta - \frac{\boldsymbol{n} \cdot d\boldsymbol{h}}{dS} \tag{21}$$

228   Order

229
$$\sigma_0 = \left(\gamma H_u + \gamma' H_w\right)\cos^2\theta - n_p\gamma_w H_w\cos\theta\sin\xi - n_e k_c\left(\gamma H_u + \gamma_{sat}H_w\right)\cos\theta,$$
$$h_n = -\frac{\boldsymbol{n}\cdot d\boldsymbol{h}}{dS}$$
(22)

230   Therefore

231
$$\sigma = \sigma_0 + h_n$$
(23)

232   Here, σ_0 = contribution of volume force to the normal stress. h_n = contribution

233   of the force of surrounding soil to the normal stress of sliding surface.

234   The normal stress distribution of the slip surface can be approximated in the

235   following (Zheng, 2009):

236
$$\sigma = \sigma_0 + f(x, y; \boldsymbol{a})$$
(24)

237   where $f(x, y; \boldsymbol{a})$ = function in the horizontal coordinates (x, y) with a parametric

238   vector $\boldsymbol{a}$ consisting of five unknowns. $f(x, y; \boldsymbol{a})$ is constructed by piecewise triangular

239   linear interpolation:

240
$$f(x, y; \boldsymbol{a}) = \boldsymbol{la}$$
(25)

241   where $\boldsymbol{l}$ is the interpolation function, $\boldsymbol{l} = \left(l_1, l_2, ..., l_5\right)$, and it satisfies $\sum_{i=1}^{5} l_i = 1$.
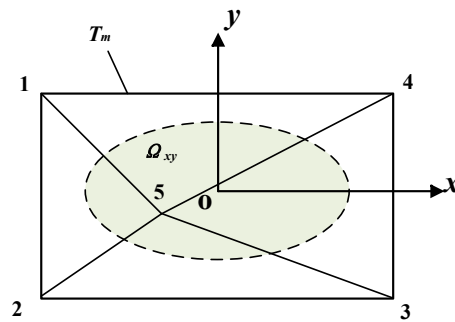
243   **Fig. 7** A triangular mesh for interpolation of normal stress on slip surface

244   As shown in Fig. 7, Ω_{xy} is the projection of the sliding body on the *xoy* plane, the

245   area characterized by the dashed line. T_m is a triangular network containing 5 nodes.

246     $l_i(x, y)(i = 1, 2, ..., 5)$ is the interpolation function for these 5 nodes, which can be

247 formed as in finite elements with the help of the area coordinates of the 4 triangles on

248 T_m.

249   Substitute Eq. (24) into Eq. (17), a system of nonlinear equations with F_s and $\boldsymbol{a}$ as

250 unknowns is obtained:

251 $$F_s \boldsymbol{Ba} + \boldsymbol{Da} + F_s \boldsymbol{b} + \boldsymbol{d} = 0 \tag{26}$$

252   Where $\boldsymbol{B}$ and $\boldsymbol{D}$ are both matrices of order 6×5, and $\boldsymbol{b}$ and $\boldsymbol{d}$ are both vectors of

253 order six, whose expressions are respectively.

254
$$\begin{cases} \boldsymbol{B} = \iint_s \boldsymbol{n}' \boldsymbol{l} dS \\ \boldsymbol{D} = \iint_s f' \boldsymbol{s}' \boldsymbol{l} dS \\ \boldsymbol{b} = \boldsymbol{f}_m + \iint_s \sigma_0 \boldsymbol{n}' dS \\ \boldsymbol{d} = \iint_s \left(c_w + f' \sigma_0 \right) \boldsymbol{s}' dS \end{cases} \tag{27}$$

255   We can solve Eq. (26) by either Newton's method or eigenvalue method.

256   In Eq. (26), all terms except the resultant external force (moment) $\boldsymbol{f}_m$ are area

257 integrals. The volume integrals on the sliding body involved in the problem are

258 transformed into boundary integrals that can skip the column partitions. Hence, it is not

259 required to divide the sliding body into columns anymore, only the surface of the sliding

260 body needs to be partitioned, as detailed in Zheng (2007).

261 **4 Verification examples**

262   In order to verify the accuracy of the proposed method, two examples are analyzed

263 in this section. Different working conditions were set up for Example 2 and the results

264 are compared with those calculated by the software.

4.1 Example 1: translational sliding

Wedge stability in rock mechanics is a typical 3D limit equilibrium analysis problem. Examples of wedge include two cases of geometric symmetry and asymmetry. Example 1 is an asymmetric wedge. Fig. 8 shows the three-dimensional model and geometric parameters of the wedge plane sliding. The sliding surface is composed of two structural planes, ABC and OAB, and the coordinates of the vertices have been listed in Fig. 8. The sliding direction of the wedge sliding body is assumed to be parallel to the intersection line AB. The sliding surface of the wedge adopt the same shear strength: $c' = 50\text{kPa}$ and $\varphi' = 30°$. The unit weight of the wedge is 26 kN/m³. For simple wedges, the 3D limit equilibrium method has analytical solutions, but these methods all include an assumption that the shear force on the bottom slip plane is parallel to the intersecting prism. If the sliding direction of the wedge sliding body is assumed to be parallel to the intersection line AB of the two structural planes, the wedge sliding body is statically determinate, and the safety factor has an exact value of 1.640 (Hoek and Bray, 1977) for this example. The safety factor calculated based on the method in this paper is 1.652. This discrepancy may stem from the triangulation of the sliding surface. In our method, the sliding surface is approximated using a series of small triangular elements, which might introduce a slight inaccuracy, leading to a minor deviation in the calculated safety factor. However, we observed a slight difference between exact value and the result obtained by the method proposed in our study, it demonstrates that the proposed method can reasonably evaluate the stability of rocky

286   slopes containing different structural surfaces.
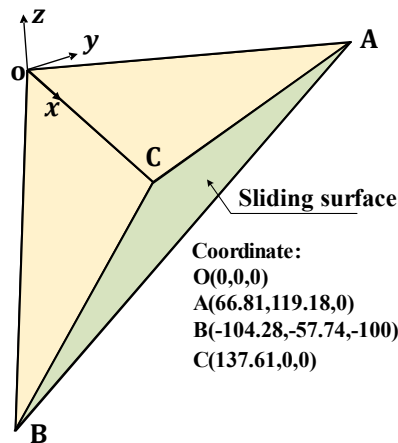
Fig. 8 Model and geometric parameters of the wedge

4.2 Example 2: ellipsoidal sliding

290   In order to verify the feasibility of the proposed method for calculating the slope

291   stability under seepage and earthquake, a classical ellipsoid example is selected for the

292   stability analysis, as shown in Fig.9, which is derived from the study of Zhang (1988).

293   Zhang's (1988) paper in 1988 provides a three-dimensional slope ellipsoid slip surface

294   example, and the simplified three-dimensional limit equilibrium method (only three

295   force equilibrium and one moment equilibrium are satisfied) is used for the stability

296   analysis. Zhang's (1988) solution for the 3D limit equilibrium of a symmetric ellipsoid

297   can be regarded as a rigorous solution since the ellipsoid has a symmetric sliding

298   surface and the other two moment equilibrium conditions are automatically satisfied by

299   the symmetric bar-column method. Zhang's (1988) solution has also been used by many

300   scholars to check the correctness of their own procedures (Hungr et al., 1989; Huang

301   and Tsai, 2000; Zheng, 2009). The example is a homogeneous slope, the potential

302   sliding surface is a part of a simple ellipsoid, the sliding surface is symmetric about the

303 *xoz* plane, and the equation of the sliding surface is

$$\left(\frac{x\text{-}36.6}{24.4}\right)^2 + \left(\frac{y}{66.9}\right)^2 + \left(\frac{z\text{-}27.4}{24.4}\right)^2 = 1 \qquad (26)$$

304
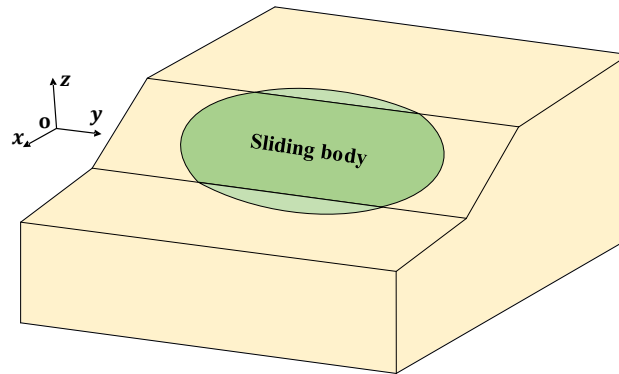
305

306        **Fig. 9** Model of ellipsoid example
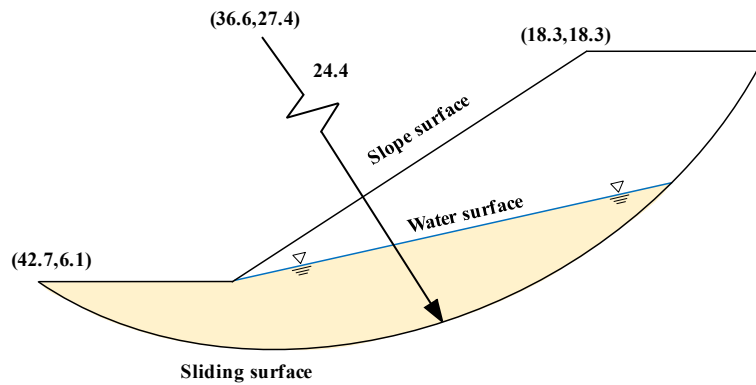
307

308    **Fig. 10** Geometric parameters and middle profile with groundwater

309    The ellipsoid model is shown in Fig. 9. The external load of the slope is only

310 considered the effect of gravity, the unit gravity is 19.2kN/m3, and the effective shear

311 strength parameter: $c' = 29.3\text{kPa}$ and $\varphi' = 20°$. We extended the analysis to include

312 complex conditions such as groundwater presence and seismic activity. Four working

313 conditions are considered in this section, case-1: no groundwater is considered as in the

314 computational model of Zhang (1988); case-2: groundwater is set up as shown in Fig.

315 10, the mechanical parameters are listed in Table 1; case-3: earthquake action in the

horizontal direction is considered; case-4: both groundwater and horizontal earthquake

action are considered. Reference to the peak ground acceleration at the location of the

real slope in the Three Gorges reservoir area in Section 5, the earthquake acceleration

is taken 0.05g and the horizontal earthquake direction along the x-axis positive direction.

The results from other methods and our proposed method are listed in Table 2.

Table 1 Mechanical parameters of the slope

Unit weight, γ (KN/m³)		Shear strength, c' (kPa)		Friction angle, φ' (°)	
Saturated condition	Unsaturated condition	Saturated condition	Unsaturated condition	Saturated condition	Unsaturated condition
21	19.2	15.8	29.3	13.5	20

Case-1: The safety factor calculated using our proposed method is 2.054, whereas

Zhang (1988) obtained a result of 2.122 using the limit equilibrium method.

Additionally, we perform a 2D stability analysis of the intermediate cross-section of the

model using Rocscience's Slide software and obtain a safety factor of 2.084. Comparing

the results mentioned above, it becomes evident that our proposed method for slope

stability analysis is feasible, and its calculation results are consistent with the results

obtained by using the traditional limit equilibrium method and two-dimensional

stability analysis.

Case-2: Only the effect of groundwater seepage is considered. Mechanical

parameters of the slope below the water surface adopt saturated, while above the water

surface adopt unsaturated. The groundwater not only induces hydrodynamic effects, but

also increases the saturation of geotechnical materials, leading to a reduction in soil

334 shear strength. In this working condition, the calculated safety factor is 1.183, which is

335 close to 1.057 calculated by Rocscience's Slide.

336 Case-3: We only consider the effect of horizontal earthquake on slope stability. In

337 order to compare the results with the 2D stability calculations, we choose the horizontal

338 seismic action direction to be in the *xoz* plane. The results calculated by the 3D

339 procedure and the 2D software are 1.855 and 1.861, respectively. Compared with the

340 case-2, the effect of seepage on the slope stability is greater than that of seismic action.

341 Case-4: We considered both seepage and horizontal seismic effects. In this case,

342 the results calculated by 3D program and 2D software are 1.047 and 0.934 respectively.

343

Table 2 Safety factor of Example 2

Method	Zhang (1988)	Slide(2D)	The proposed method
Case-1	2.122	2.084	2.054
Case-2	-	1.057	1.183
Case-3	-	1.861	1.855
Case-4	-	0.934	1.047

344 Based on the above calculation results, the comparison revealed minimal

345 differences across all four conditions (natural, with groundwater, with seismic loading,

346 and combined), indicating that the proposed method is also effective in assessing slope

347 stability under seepage and seismic actions.

348 **5 A True 3D Slope**

349 This section investigates slope stability evolution under the influence of rainfall

350 and earthquake by taking an actual slope in the Three Gorges reservoir as a case study.

351

352   **Fig. 11** Geographical location map of Woshaxi slope (© Google Maps)
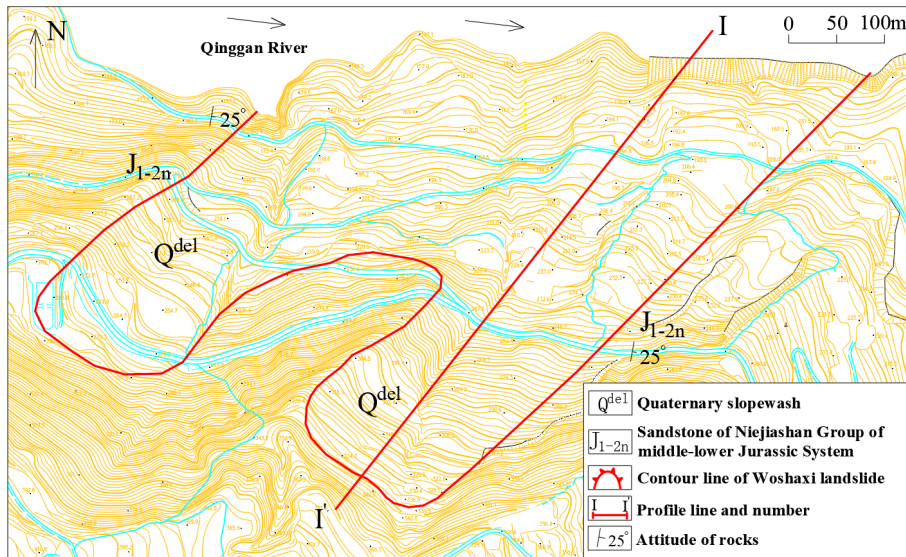
353

354   **Fig. 12** Contour map of Woshaxi slope
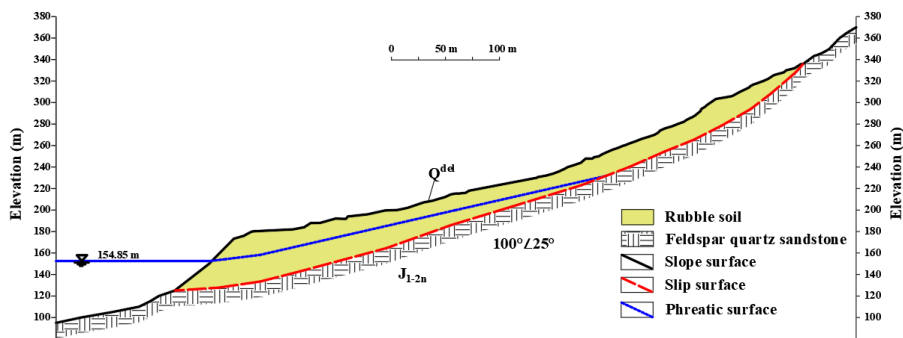
355

356   **Fig. 13** Geological section map of Woshaxi slope

357   Fig. 11 provides a depiction of the Woshaxi landslide's geographical setting. Fig.

12 shows a topographic map of Woshaxi slope with contour lines and the cross-section (I-I') of the landslide is illustrated in Fig. 13. This landslide is located on the right bank of the Qinggan River, a Yangtze River tributary, and lies about 1.5km away from the Qianjiangping landslide situated on the river's opposite bank. The composition of the Woshaxi landslide primarily consists of rubble and soil, underlain by Jurassic-era sandstone and mudstone layers that are interstratified. The orientation of these rock layers is $100° \angle 25°$. The landslide has experienced significant impact due to water level fluctuations in the range of 145-175m, resulting in submersion of its frontal part by about 20-50m. This geological structure displays a descending gradient from the southwest to the northeast, with a general gradient of 20°. The highest point at the rear reaching an elevation of 405m, and the front edge descending below 140m. The landslide encompasses an average thickness of around 15m and a total volume estimated at 4.2×10^6 m^3. Its main sliding direction of the landslide body is toward 40° east of north.

According to the Seismic Ground Motion Parameter Zonation Map of China, the peak ground motion acceleration in this region is 0.05g. To investigate slope stability evolution under seismic conditions, peak accelerations are calculated and analyzed at various levels. The most dangerous case is considered in the following calculations, where the direction of the horizontal seismic action coincides with the primary sliding direction. The precipitation pattern in this region is characterized by relatively concentrated temporal and spatial distribution. Most of the rainfall occurs between

379   April and October. To investigate the stability of three-dimensional slopes under the

380   combined influence of rainfall and earthquake, this study considers the effects of three

381   geotechnical parameters: permeability coefficient, porosity, and saturation. The

382   proposed method is applied to calculate changes in slope stability resulting from

383   average monthly rainfall and earthquake occurring between 2007-2009.
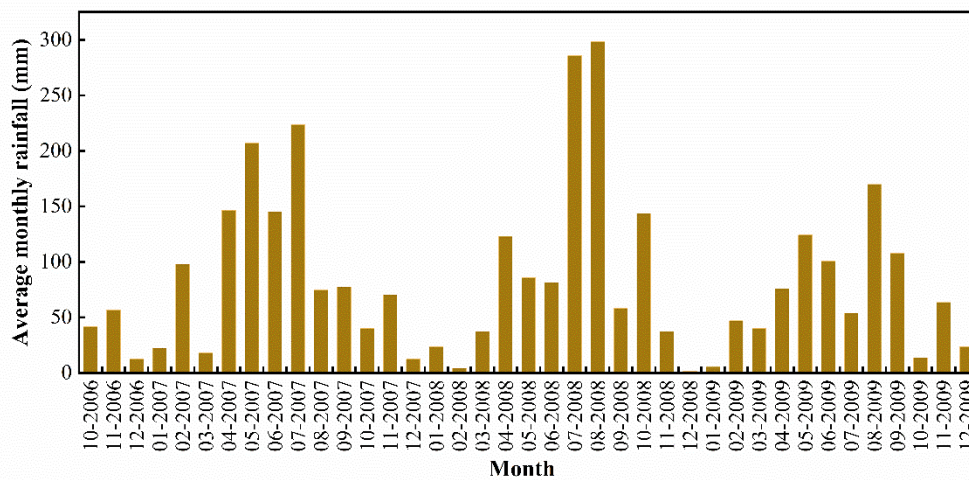
384

385   **Fig. 14** Average monthly rainfall from 2007 to 2009

386   Fig. 14 shows the average monthly rainfall from 2007 to 2009. Table 3 lists the

387   physical and mechanical parameters of the landslide body. It is assumed that the

388   reservoir water level remains unchanged. To assess the effects of different geotechnical

389   parameters and seismic action on the safety factor, four cases are considered: (i) rainfall

390   only, (ii) rainfall and horizontal earthquake, (iii) rainfall and vertical earthquake, and

391   (iv) rainfall and earthquake in both horizontal and vertical directions.

392   **Table 3** Mechanical parameters of Woshaxi slope

Unit weight,γ (KN/m³)		Shear strength,$c^{'}$ (kPa)		Friction angle,$\varphi^{'}$ (°)	
Saturated condition	Natural condition	Saturated condition	Natural condition	Saturated condition	Natural condition

22.4	20.8	18	22	15	20

(i) Rainfall only

The three parameters, infiltration coefficient, porosity, and saturation, have different effects on the safety factor of slopes. The safety factor varies with the monthly rainfall. The analysis indicates that an increase in rainfall does not invariably lead to a decrease in the safety factor of the slope. This phenomenon can be attributed to the fact that increased rainfall raises the phreatic surface within the slope, affecting two key aspects: firstly, it enhances the hydrodynamic forces, and secondly, it increases the pressure at the base of the slope. When the increase in pressure at the slope's base has a more pronounced impact on stability than the hydrodynamic forces, the safety factor of the slope will subsequently increase. Conversely, if the hydrodynamic forces dominate, the stability of the slope will diminish. As shown in Fig. 15(a), the permeability coefficient k is 0.01, 0.1 and 1m/d, respectively. With other parameters unchanged, the trend of safety factor variation for Woshaxi landslide is consistent. The higher the permeability coefficient, the greater the soil's ability to allow water to pass through above the phreatic surface, the smaller the rise of the phreatic surface within the slope. This results in a smaller increase in pressure at the foot of the slope and a lower safety factor.

As shown in Fig. 15(b), the porosity n is 0.1, 0.3 and 0.5, respectively, and the safety coefficient of the Woshaxi landslide is consistent under the condition that other parameters remain unchanged. The higher the porosity, the greater the soil permeability above the phreatic surface, the smaller the rise of the phreatic surface within the slope,

414   resulting in a smaller increase of pressure at the slope's foot and thus a lower safety

415   factor.

416   As shown in Fig. 15(c), the saturation S_r of the soil above the phreatic surface of

417   the landslide is 0.4, 0.6 and 0.8, respectively, and the safety factor of the Woshaxi

418   landslide is consistent under other parameters remained unchanged. The higher the

419   saturation, the lower the permeability of soil above the phreatic surface, resulting in a

420   greater rise of phreatic surface within the slope and an increased pressure at its foot,

421   thereby leading to a higher safety factor. Overall, under rainfall conditions, soil porosity

422   on the phreatic surface has a greater impact on safety factor than permeability

423   coefficient and saturation.
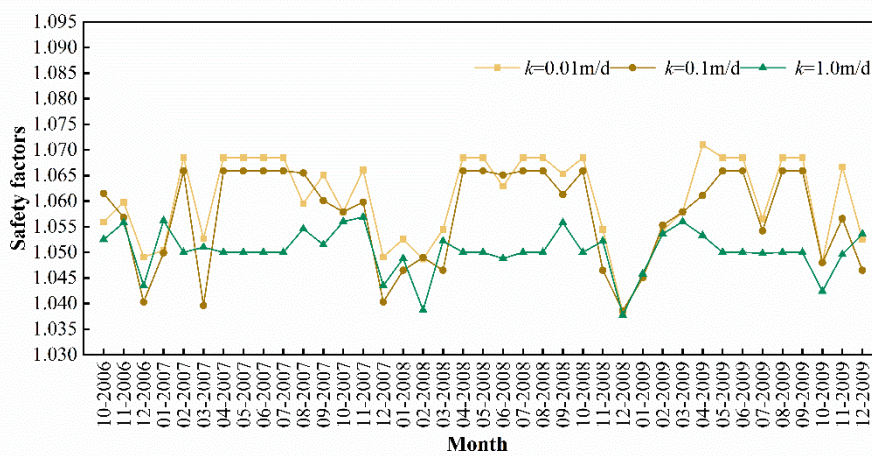
424

425   (a) permeability coefficient
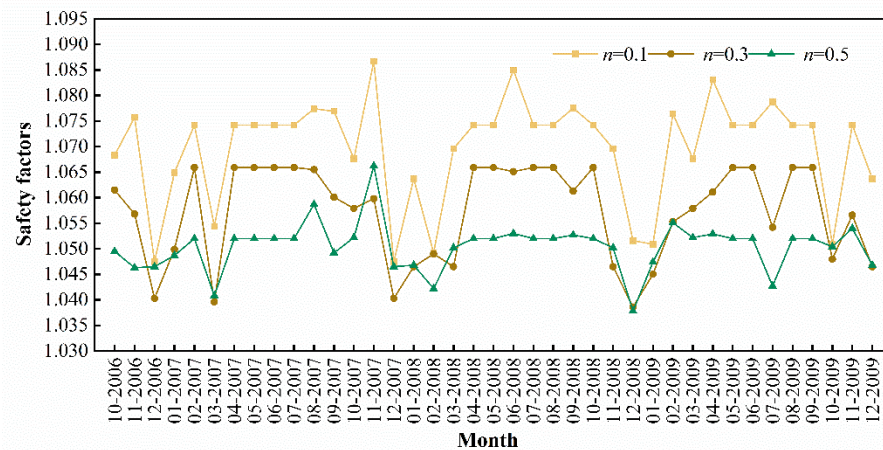
426

427   (b) porosity
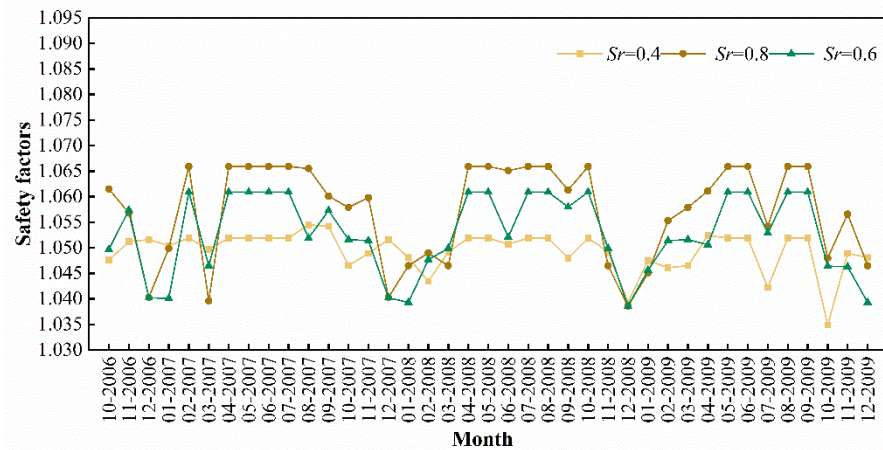
428

429   (c) saturation

430   **Fig. 15** Safety factors of the Woshaxi landslide under rainfall

431   (ii) Rainfall and horizontal earthquake

432   Fig. 16 shows the evolution of the stability of the Woshaxi landslide under the

433   combined effect of rainfall and horizontal earthquake with different geotechnical

434   parameters, and the horizontal earthquake coefficient k_h is taken as 0.05. Comparing

435   with Fig. 15, it can be observed that after considering the effect of horizontal earthquake,

436   the variation trend of the safety factor of the Woshaxi landslide calculated with different

437   geotechnical parameters is consistent with that under the rainfall condition only, but the

438 stability of the landslide is obviously decreased. Fig. 17 shows the evolution of the

439 stability of the Woshaxi landslide with rainfall and different horizontal earthquake

440 coefficients. With other parameters unchanged, the values of the horizontal earthquake

441 coefficients are 0.05, 0.1 and 0.15 respectively. In this research, we employed three

442 different horizontal earthquake coefficients: 0.05, 0.1, and 0.15. The coefficient of 0.05

443 is based on the seismic zoning map of China, corresponding to the seismic

444 characteristics and expected level of seismic activity in the study area. As for the other

445 two coefficients, 0.1 and 0.15, they are not directly associated with any specific

446 earthquake magnitude or return period. These values were set based on engineering

447 requirements and safety considerations, aiming to assess the variation in slope stability

448 under stronger seismic actions. This approach allows us to understand the response of

449 the slope under different seismic intensities and provides a safety margin for seismic

450 activities that may exceed expectations. Our study has revealed that within the specific

451 context of the examined landslide, as the horizontal earthquake coefficient increases,

452 there is a notable decrease in the safety factor. It is also observed that in this particular

453 case, the impact of seismic activity on slope stability appears to be considerably more

454 pronounced than that of rainfall. However, these findings are derived from a singular

455 case study, focusing on a specific landslide morphology and set of soil properties.

456 Consequently, they may not necessarily be universally applicable across different

457 landslide types and varying geological conditions.
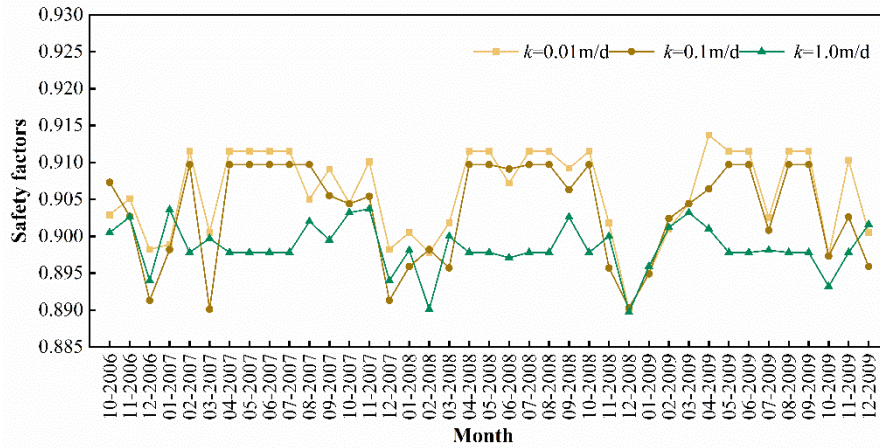
459   (a) permeability coefficient
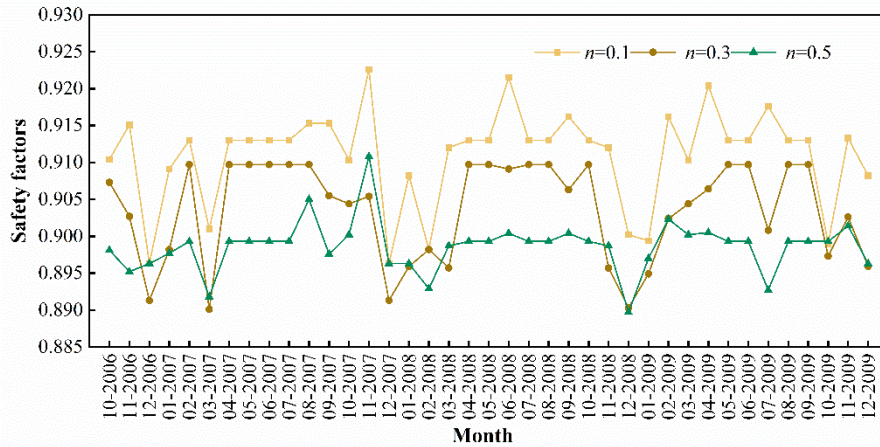
461   (b) porosity
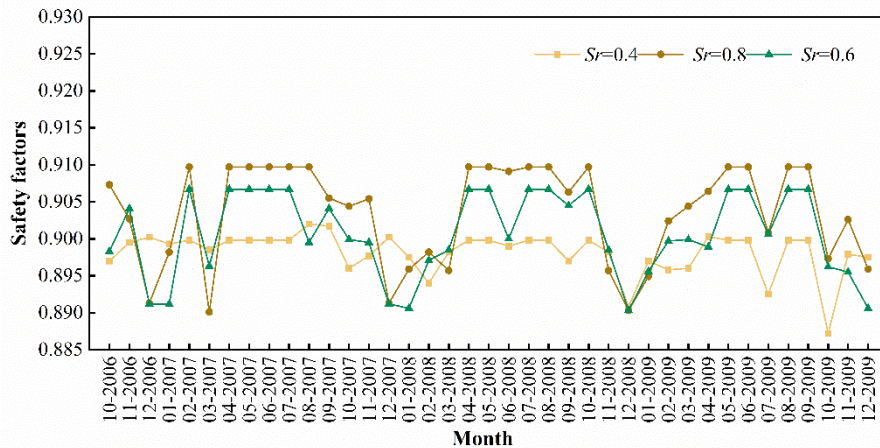
463   (c) saturation

464   **Fig. 16** Safety factors of the Woshaxi landslide under rainfall and horizontal

465   earthquake (k_h = 0.05)
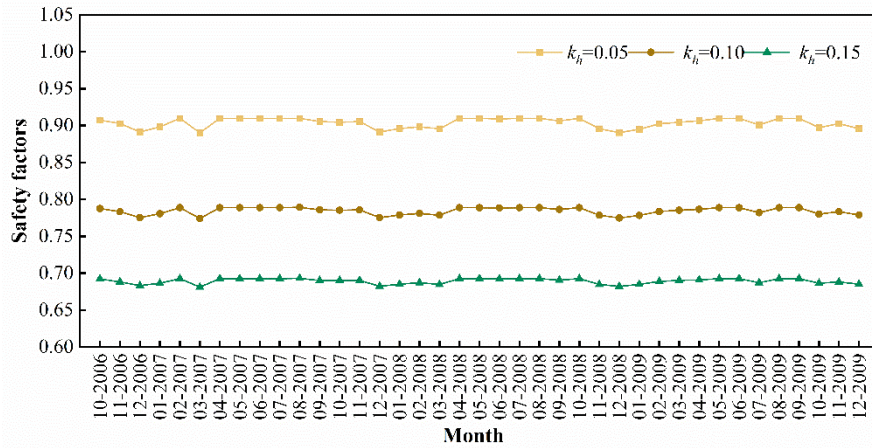
466

467 **Fig. 17** Safety factors of the Woshaxi landslide under rainfall and horizontal

468 earthquake (different horizontal seismic coefficient)

469 (iii) Rainfall and vertical earthquake

470 Fig. 18 shows the evolution of the stability of the Woshaxi landslide with rainfall

471 and different vertical earthquake coefficients. With other parameters unchanged, the

472 vertical earthquake coefficient k_v takes on values of 0.025, 0, and -0.025 respectively,

473 and the negative sign indicates that the direction of vertical earthquake is vertically

474 downward. It is obvious from Fig. 18 that the corresponding safety factor when the

475 earthquake acts vertically downward is smaller than the corresponding safety factor

476 when it is vertically upward.
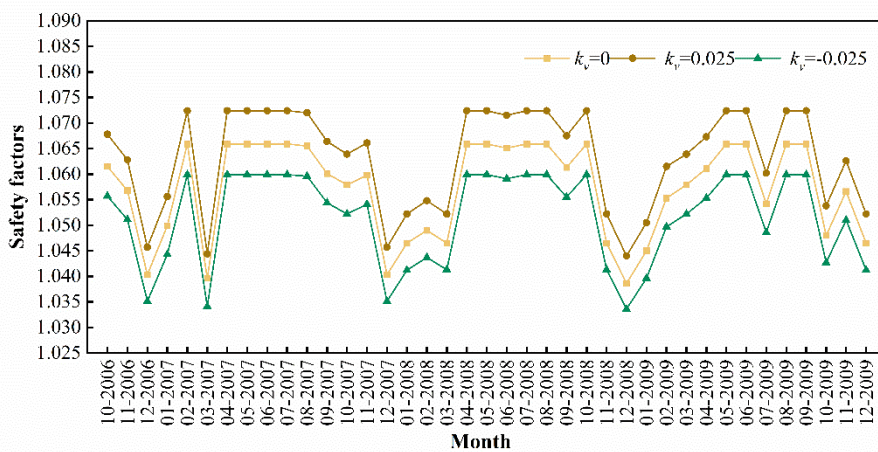
477

478 **Fig. 18** Safety factors of the Woshaxi landslide under rainfall and vertical earthquake

479 (iv) Rainfall and earthquake in both horizontal and vertical directions

480 Fig. 19 shows the evolution of the stability of the Woshaxi landslide with rainfall

481 and different earthquake coefficients. Horizontal earthquake coefficient k_h is taken as

482 0.05, and the values of vertical earthquake coefficient are 0.025, 0, -0.025 respectively,

483 and the negative sign indicates that the direction of vertical earthquake action is

484 vertically downward. Under the condition that other parameters remain unchanged, the

485 slope stability is lower when considering both horizontal and vertical upward

486 earthquake compared to considering only horizontal earthquake. Therefore, it is

487 essential to properly account for the effect of vertical earthquake in order to ensure

488 maximum safety.
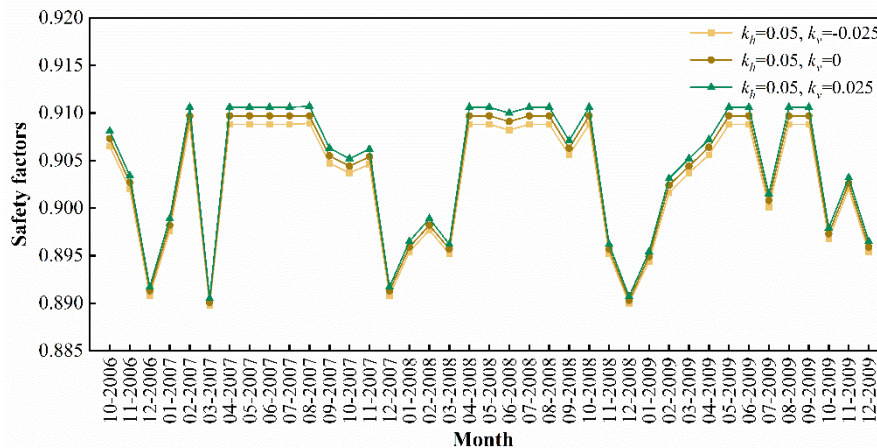
489

490 **Fig. 19** Safety factors of the Woshaxi landslide under rainfall and earthquake (in both

491 horizontal and vertical directions)

6 Conclusions

493 In this paper, the calculation of the seepage force is studied, the normal stress

494 expression on the sliding surface of a slope under seepage force and seismic force are

also derived. Furthermore, a global analysis method that considers both seepage and seismic forces is proposed to determine the safety factor of slopes subjected to the combined effect of rainfall and earthquake. The reliability of the proposed method is also verified with two examples combining software calculations and previous results.

Taking a slope in the Three Gorges reservoir area as an example, this study investigates the influence of soil permeability coefficient, porosity and saturation on slope stability, and analyzes the safety evolution of this slope under combined effects of rainfall and earthquake. The results indicate that, under rainfall conditions, the porosity of the soil above the phreatic surface exerts a greater influence on safety factor than permeability coefficient and saturation. With an increase in the horizontal earthquake coefficient, the safety factor of the landslide is significantly reduced, and the impact of earthquake on slope stability surpasses that of rainfall. The safety factor corresponding to vertical downward earthquake action is smaller than that of vertical upward, and the stability of slope is lower when considering horizontal and vertical upward earthquake actions. Therefore, in order to ensure maximum safety, proper consideration should be given to vertical earthquake actions.

When considering rainfall alone, the slope safety factor is 1.04-1.09, positioning the slope in a state that between unstable and basically stable. However, upon accounting for horizontal seismic activity, the slope safety factor decreases to about 0.9 and is transformed into an unstable state. When the vertical earthquake is considered, the slope safety factor is 1.035-1.075. This represents a slight reduction but still in the

unstable and basically stable state. This suggests that horizontal seismic influences exert a more pronounced impact on slope stability compared to vertical. When rainfall and earthquake act simultaneously, the safety factor calculated using the proposed method falls below 1.0, indicating an unstable condition where landslide disasters are likely to occur on the slope. The research results provide scientific basis for slope stability analysis and prevention. Further, the proposed method can identify potential risk areas for landslide hazards, and planners in the Three Gorges Reservoir area can better consider these risks and take measures to increase the seismic and flood resilience of reservoir infrastructure.

Data availability

The data used in this study are available from the first author upon request.

Author contribution

JW analyzed the data, conceived the paper, and wrote the paper; ZW conceived and co-wrote the paper; HL reviewed and improved the analysis and paper; and GS provided the data of the actual slope in the Three Gorges reservoir.

Competing interests

The contact author has declared that none of the authors has any competing interests.

Acknowledgments

This study was supported by the National Natural Science Foundation of China (Grant No.11972043).

References

Ali, A., Lyamin, A. V., Huang, J., Li, J. H., Cassidy, M. J., Sloan, S. W. 2016. Probabilistic stability assessment using adaptive limit analysis and random fields. Acta Geotechnica, 12(4), 937–948, https://doi.org/10.1007/s11440-016-0505-1.

Bishop, A.W. 1955. The use of the slip circle in the stability analysis of slopes. Geotechnique 5 (1): 7-17.

Cao, L.C., Zhang, J.J., Wang, Z.J., Liu, F.C., Liu, Y., Zhou, Y.Y. 2019. Dynamic response and dynamic failure mode of the slope subjected to earthquake and rainfall. Landslides 16, 1467-148, https://doi.org/10.1007/s10346-019-01179-7.

Chang, K.T., Lin, M.L., Dong, J.J., Chien, C.H. 2012. The hungtsaiping landslides: from ancient to recent. Landslides 9(2): 205-214, https://doi.org/10.1007/s10346-011-0293-5.

Chen, Z.Y. 2001. A three-dimensional limit equilibrium method for slope stability analysis. Chinese Journal of Geotechnical Engineering (05): 525-529.

Cheng, Y.M., Yip, C. J. 2007. Three-Dimensional Asymmetrical Slope Stability Analysis Extension of Bishop's, Janbu's, and Morgenstern–Price's Techniques. Journal of Geotechnical and Geoenvironmental Engineering 133(12): 1544-1555, https://doi.org/10.1061/(asce)1090-0241(2007)133:12(1544).

Chopra, A.K. 1966. The importance of the vertical component of earthquake motions. Bulletin of the Seismological Society of America 56(5): 1163-1175.

Conte, E., Troncone, A. 2017. A simplified method for predicting rainfall-induced

558   mobility of active landslides. Landslides. 14(1): 35-45, https://doi.org/10.1007/s10346-

559   016-0692-8.

560   David, K.K. 2000. Statistical analysis of an earthquake-induced landslide distribution-

561   the 1989 Loma Prieta, California event. Engineering Geology 58(3-4): 231-249,

562   https://doi.org/10.1016/s0013-7952(00)00037-5.

563   Farzaneh, O., Askari, F., Ganjian, N. 2008. Three-Dimensional Stability Analysis of

564   Convex Slopes in Plan View. Journal of Geotechnical and Geoenvironmental

565   Engineering 134(8): 1192-1200, https://doi.org/10.1061/(asce)1090-

566   0241(2008)134:8(1192).

567   Griffiths, D.V., Lane, P. A. 1999. Slope stability analysis by finite elements.

568   Geotechnique 49 (3): 387-403.

569   Guo, M.W., Ge, X.R., Wang, S.L., Wang, H. 2011. Dynamic stability analysis of slope

570   based on vector sum analysis method. Chinese Journal of Rock Mechanics and

571   Engineering 30(3): 572-579.

572   Hoek, E., Bray, J.W., 1977. Rock Slope Engineering. The Institute of Mining and

573   Metallurgy, London.

574   Huang, C. C., Tsai, C. C. 2000. New Method for 3D and Asymmetrical Slope Stability

575   Analysis. Journal of Geotechnical and Geoenvironmental Engineering, 126(10), 917–

576   927, https://doi.org/doi:10.1061/(asce)1090-0241(2000)126:10(917).

577   Hungr, O. 1987. An extension of Bishop's simplified method of slope stability analysis

578   to three dimensions. Geotechnique 37(1): 113-117,

https://doi.org/10.1680/geot.1987.37.1.113.

Ishii, Y., Ota, K., Kuraoka, S., Tsunaki, R. 2012. Evaluation of slope stability by finite element method using observed displacement of landslide. Landslides 9(3), 335-348, https://doi.org/10.1007/s10346-011-0303-7.

Iverson, R.M. 2000. Landslide triggering by rain infiltration. Water Resources Research 36(7): 1897-1910, https://doi.org/10.1029/2000WR900090.

Jibson, R.W., Harp, E.L. 2016. Ground Motions at the Outermost Limits of Seismically Triggered Landslides. Bulletin of the Seismological Society of America 106(2): 708-719, https://doi.org/10.1785/0120150141.

Lew, M. 1991. Characteristics of Vertical Ground Motions Recorded During the Lorna Prieta Earthquake. Geotechnique 41(1): 35-39.

Lim, K., Li, A. J., Schmid, A., Lyamin, A. V. 2017. Slope-Stability Assessments Using Finite-Element Limit-Analysis Methods. International Journal of Geomechanics, 17(2), 06016017, https://doi.org/10.1061/(asce)gm.1943-5622.0000715.

Ling, H.I., Mohri, Y., Kawabata, T. 1999. Seismic analysis of sliding wedge: extended Francais-Culmann's analysis. Soil Dynamics and Earthquake Engineering 18(5): 387-393, https://doi.org/10.1016/s0267-7261(99)00005-6.

Liu, L. P., Lei, Z.Y., Zhou, F.C. 2001. The evaluation of seismic slope stability analysis methods. Journal of Chongqing Jiaotong University 20(3): 83-88.

Marc, O., Meunier, P., Hovius, N. 2017. Prediction of the area affected by earthquake-induced landsliding based on seismological parameters. Natural Hazards and Earth

600   System Sciences 17(7): 1159-1175, https://doi.org/10.5194/nhess-17-1159-2017.

601   Michalowski, R.L. 1995. Slope stability analysis: a kinematical approach.

602   Geotechnique 45 (2): 283-293.

603   Morgenstern, N.R., Price, V. E. 1965. The analysis of the stability of general slip

604   surfaces. Geotechnique 15: 79-93, https://doi.org/10.1680/geot.1965.15.1.79.

605   Qin, C.B., Chian, S.C. 2018. Kinematic analysis of seismic slope stability with a

606   discretisation technique and pseudo-dynamic approach: a new perspective.

607   Geotechnique 68 (6): 492-503.

608   Rahardjo, H., Nio, A.S., Leong, E.C., Song, N.Y. 2010. Effects of Groundwater Table

609   Position and Soil Properties on Stability of Slope during Rainfall. Journal of

610   Geotechnical and Geoenvironmental Engineering 136(11): 1555-1564,

611   https://doi.org/10.1061/(asce)gt.1943-5606.0000385.

612   Salinas-Jasso, J.A., Ramos-Zuniga, L.G., Montalvo-Arrieta, J.C. 2019. Regional

613   landslide hazard assessment from seismically induced displacements in Monterrey

614   Metropolitan area, Northeastern Mexico. Bulletin of Engineering Geology and the

615   Environment 78(2): 1127-1141, https://doi.org/10.1007/s10064-017-1087-3.

616   Sassa, K., Nagai, O., Solidum, R., Yamazaki, Y., Ohta, H. 2010. An integrated model

617   simulating the initiation and motion of earthquake and rain induced rapid landslides

618   and its application to the 2006 Leyte landslide. Landslides 7(3): 219-236,

619   https://doi.org/10.1007/s10346-010-0230-z.

620   Sepúlveda, S. A., Murphy, W., Jibson, R.W., Petley, D.N. 2005. Seismically induced

621 rock slope failures resulting from topographic amplification of strong ground motions:

622 The case of Pacoima Canyon, California. Engineering Geology 80(3-4): 336–348,

623 https://doi.org/10.1016/j.enggeo.2005.07.004.

624 Shukha, R., Baker, R. 2008. Design implications of the vertical pseudostatic coefficient

625 in slope analysis. Computers and Geotechnics 35(1): 86-96,

626 https://doi.org/10.1016/j.compgeo.2007.01.005.

627 Spencer, E. 1967. A method of analysis of the stability of embankments assuming

628 parallel inter-slice forces. Geotechnique 17: 11-26. doi:10.1680/geot.1967.17.1.11.

629 Sun, G.H., Cheng, S.G., Jiang, W., Zheng, H. 2016a. A global procedure for stability

630 analysis of slopes based on the morgenstern-price assumption and its applications.

631 Computers and Geotechnics 80(dec.): 97-106,

632 https://doi.org/10.1016/j.compgeo.2016.06.014.

633 Sun, G.H., Yang, Y.T., Jiang, W., Zheng, H. 2017. Effects of an increase in reservoir

634 drawdown rate on bank slope stability: a case study at the three gorges reservoir, China.

635 Engineering Geology 221: 61-69, https://doi.org/10.1016/j.enggeo.2017.02.018.

636 Sun, G., Zheng, H., Huang, Y., Li, C. 2016b. Parameter inversion and deformation

637 mechanism of Sanmendong landslide in the Three Gorges Reservoir region under the

638 combined effect of reservoir water level fluctuation and rainfall. Engineering Geology

639 205: 133-145, https://doi.org/10.1016/j.enggeo.2015.10.014.

640 Wang, H.L., Xu, W.Y. 2005. 3D dynamical response analysis of high rock slope related

641 to hydropower project in high intensive seismic region. Chinese Journal of Rock

Mechanics and Engineering 24(2): 5890-5895.

Yin, K., Liu, Y., Wang, Y., and Jiang, Z. 2012. Physical model experiments of landslide-induced surge in Three Gorges Reservoir. Earth Science Journal China University Geoscience, 37(5): 1067-1074.

Zhang, X. 1988. Three-dimensional stability analysis of concave slopes in plan view. Journal of Geotechnical and Geoenvironmental Engineering 114(6): 658-671. https://doi.org/10.1061/(asce)0733-9410(1988)114:6(658).

Zheng, H. 2007. A rigorous three-dimensional limit equilibrium method. Chinese Journal of Rock Mechanics and Engineering 26(8): 1529-1537. https://doi.org/10.3321/j.issn:1000-6915.2007.08.002.

Zheng, H. 2009. Eigenvalue problem from the stability analysis of slopes. Journal of Geotechnical and Geoenvironmental Engineering 135(5): 647-656, https://doi.org/10.1061/(asce)gt.1943-5606.0000071.

Zheng, Y. R., Shi, W. M., Kong, W.X. 2004. Calculation on seepage forces and phreatic surface under drawdown condition. Chinese Journal of Rock Mechanics and Engineering 23(18): 3203-3210, https://doi.org/10.16285/j.rsm.2018.1617.

Zhou, J. F., Qin, C.B. 2022. Stability analysis of unsaturated soil slopes under reservoir drawdown and rainfall conditions: steady and transient state analysis. Computers and Geotechnics 142: 104541-, https://doi.org/10.1016/j.compgeo.2021.104541.

Zhou, J., Chen, Q., Wang, J. 2017. Rigid block based lower bound limit analysis method for stability analysis of fractured rock mass considering rock bridge effects. Computers

663   and Geotechnics 86: 173-180.